Nitride Materials: Synthesis, Crystal Structures, and Optical Properties

Djahida Kerdoud[1*], Faouzia Benkafada[2], Nora Boussouf[3], Chahrazed Benhamideche[1]

[1] University 20 Août 1955, BP 26, Route d'El Hadaiek Skikda 21000, Algeria
[2] University Frères Mentouri Constantine 1, BP 325, Route Ain El Bey, Constantine 25017, Algeria
[3] University Centre Abdel Hafid Boussouf, BP 26 RP, Mila 43000, Algeria

Corresponding Author Email: d.kerdoud@centre-univ-mila.dz

ABSTRACT

Our research involves the preparation of transition metal nitrides of the composition Mn_4N, NbN, Mo_2N, TaN and ZrN. The synthesis of Li_3N binary alkali metal nitride was also part of this work. Simple and cost-effective methods with relatively low impact on the environment have been privileged in the selection. The experimental work has focused on determining the optimum conditions of synthesis and the convenient high yield route to the desired nitrides, and ultimately improvement of the properties of the final materials. All samples were characterised by X-ray powder diffraction. Their structures will be discussed in more detail here. Optical band gap has been calculated from diffuse reflectance measurements. The air sensitivity of the nitrides was also probed.

1. INTRODUCTION

Inorganic nitride materials have received considerable interest during the past decade because of their technological importance. Compared to metal oxides or metals, the properties of the corresponding nitrides are superior in some respects. Unfortunately, the development of these materials is still limited [1] by providing many interesting challenges to the synthetic solid-state chemist. Due to nitrogen's high bond energy (941 KJ/mol), the formation of nitrogen gas requires high temperatures for activation; however, at these temperatures the M-N bonds in ionic/covalent nitrides become less stable. This is exacerbated by entropic effects, which favor lower nitrogen-to-metal ratios with increasing temperature.

Many nitrides are air and moisture sensitive, and rapidly form oxides, hydroxides and ammonia upon contact with oxygen or moisture. They must be prepared in oxygen-and water-free atmospheres to achieve high purity [2-5]. Synthetic approaches using more activated forms of nitrogen can be used to overcome the inertness of N_2, but increased exothermicity can also result in diminished stoichiometric control and the activation of deleterious competing pathways.

These stringent synthesis constraints, coupled with the poor intrinsic stabilities of nitrides, impose significant risk on the exploratory synthesis of novel nitride materials. Recent developments in the handling methods for air sensitive samples and improved diffraction techniques have led to moving forward in the area of nitride chemistry, making a large increase in research [1, 6, 7].

In this work, there have been attempts to synthesise the alkali metal nitride Li_3N and materials based on the nitrides of d-block transition metals mainly, Mn_4N, NbN, Mo_2N, TaN and ZrN. This contribution describes how nitride materials are produced using different methods. Powder X-ray diffraction with emphasis placed on the structural studies and optical band gap using UV-Vis reflectance spectroscopy are main focus in this paper.

2. MATERIALS AND METHODS

All procedures were performed in an inert atmosphere inside a glovebox equipped with a circulative purification system to prevent moisture and oxygen contaminations, in which the H_2O and O_2 concentrations were kept below 1 ppm.

Manganese nitride Mn_4N was prepared by heating Mn powder (Aldrich, 99.9%) in a flow of super pure NH_3 at 600°C for 3 h. An annealing at 500°C has been followed for 20 h in the same atmosphere.

Niobium nitride NbN nitride was synthesised by the vapor-phase reaction of gaseous niobium pentachloride ($NbCl_5$) with ammonia (NH_3) at 200-1300°C [8]. The formation process of NbN can be followed by changing heating temperature. The reaction of $NbCl_5$ with ammonia to form $NbCl_5$ and $5NH_3$ has been occurred first at around 200°C. The Nb_4N_5 was obtained at 250-950°C is considered to be due the reaction of $NbCl_5$-$5NH_3$ with ammonia above about 250°C leading to Nb_4N_5 product. Nb_4N_5 decomposes and can be converted to NbN at above 1000°C.

Molybdenum nitride Mo_2N was produced by the temperature programmed reaction method previously described [9]. Approximately 0.1 g of molybdenum (VI) oxide powder (MoO_3, Aldrich) was loaded onto a quartz wool plug in a quartz tube reactor. The oxide was first nitridated using a mixture of nitrogen/hydrogen with a predetermined temperature. After the material was cooled to room temperature, the material was passivated in a mixture of 1% O_2 in He flowing for 24 h. This step was necessary to prevent pyrophoric oxidation upon contact with air.

Tantalum nitride TaN was prepared by the reduction in liquid ammonia. The reaction of solutions of tantalum pentachloride ($TaCl_5$) with sodium was previously reported

[10]. The obtained powder was heated under vacuum at 900°C for 24 h.

Zirconium nitride ZrN was produced from Zirconium tetrachloride ($ZrCl_4$, Alfa Aesar) and ammonia (NH_3) injection using nonthermal plasma reactor [11]. The as-obtained powder was annealed at 250°C and 0.3 Torr in 90 SCCM of argon flow for 1 h to remove the ammonium salt [12].

Lithium metal foil (99.9 purity, 0.75 mm thickness) was purchased from Alfa Aesar and was used for the preparation of Li_3N. During the synthesis, about 1 g of Li metal foil was filed firstly until most of the metal oxide coating removed and a shiny surface appeared. In a recirculating glovebox filled with nitrogen, the Li metal was further filed until no oxide layer remained. After 3 days, the cleaned Li metal foil transformed spontaneously into a Li_3N flake, which was further heat-treated outside the glovebox using a furnace to ensure the metal has fully reacted with nitrogen. The direct reaction took place under N_2 gas at 200°C for 24 h. Li_3N powder was obtained after grinding using sandpaper or file.

All obtained samples Mn_4N, NbN, Mo_2N, TaN, ZrN and Li_3N, were transferred directly to the glovebox after cooling in each case, which reduce the risk of impurity phases forming. All the ground samples were stored in the glovebox for further characterisation.

3. MATERIALS CHARACTERISATION

All product powders were characterised by the standard powder X-ray diffraction (PXD) technique with a PANalytical X'Pert Pro MPD powder diffractometer (Cu K_α source, 40 kV, 40 mA). Samples were loaded in the glovebox into a bespoke aluminum sample holder consisting of a sealed chamber equipped with a Mylar window. All phase analyses were performed using the HighScore plus software. For the phase-pure samples, Rietveld refinements in diffraction patterns were conducted using the GSAS and EXPGUI packages [13, 14]. The scale factor, zero point and background were refined in initial cycles. A shifted Chebyschev polynomial function (background function 1 in GSAS) was employed to model the background. The unit cell parameters, peak profile parameters and atomic parameters were refined subsequently. The peak shape was modelled using the pseudo-Voigt function (profile function 2 in GSAS).

Powdered samples were irradiated by UV-Vis spectrophotometer. The powder was placed in the sample holder inserted into diffuse reflectance spectrometer. The praying mantis mirror was placed over the top of the sample and the sample compartment sealed for light. Scans were run in reflectance mode over the operative range 190-1300 nm. Band gap values were calculated by extrapolation of the steepest part of the curve towards the baseline, reading off at 0% in nm and converting to eV using the Kubelka-Munk approach proposed by Tauc et al. [15], and David and Mott [16].

4. RESULTS AND DISCUSSION

Analysis of PXD data for the full series of samples served to confirm their purity. Figure 1 shows the X-ray diffraction pattern of manganese nitride derived by the conventional heating method under ammonia gas. The peaks were indexed with the cubic phase of Mn_4N (ICSD#01-089-4804) and the hexagonal phase of $Mn_2N_{0.86}$ (ICSD#01-071-0200).
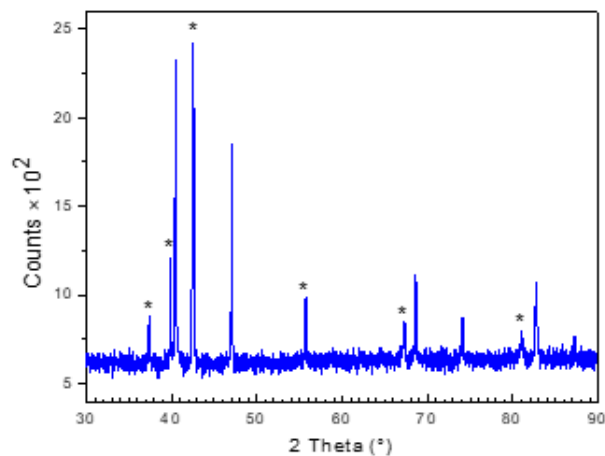
Figure 1. Powder X-ray diffraction pattern of Mn_4N. The $Mn_2N_{0.86}$ phase is indicated by the asterisks
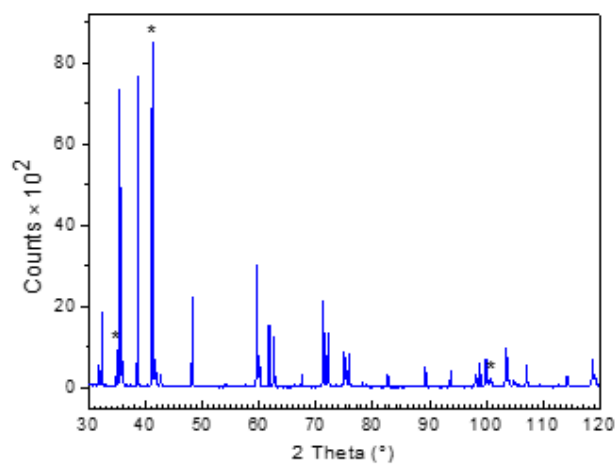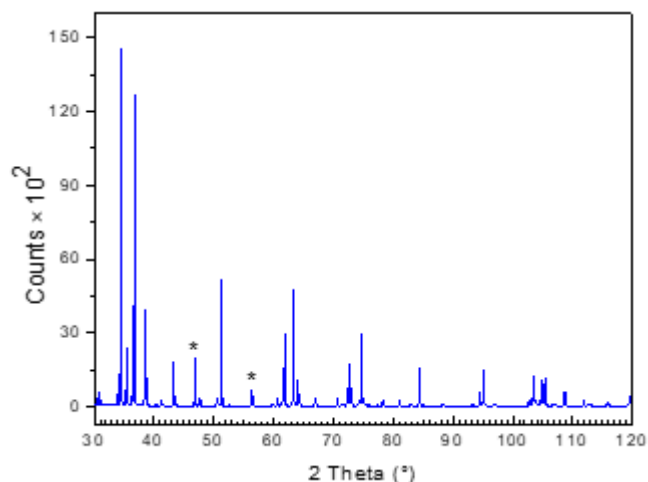

Figure 2. Powder X-ray diffraction pattern of NbN. The $Nb_8N_{6.8}$ phase is indicated by the asterisks
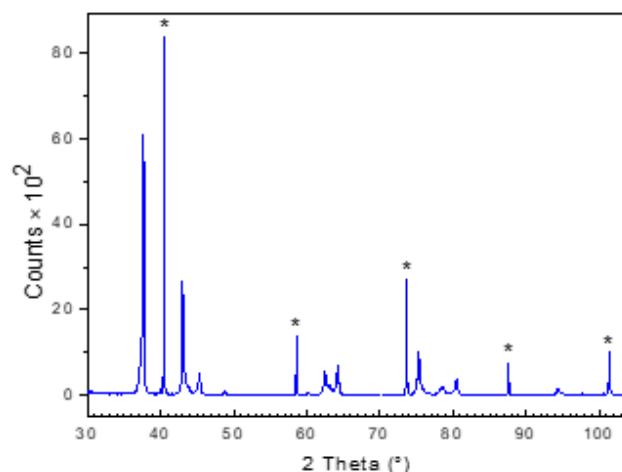
Figure 3. Powder X-ray diffraction pattern of Mo_2N. The Mo phase is indicated by the asterisks

The typical X-ray diffraction pattern of chemically prepared NbN powder, in the range of $30° \leq 2\theta \leq 120°$, is shown in Figure 2. The major feature can be indexed as a hexagonal phase of NbN (PDF#03-065-3417) with the appearance of small and moderate quantity of tetragonal $Nb_8N_{6.8}$ (PDF#03-065-2252) as second phase.

Figure 4. Powder X-ray diffraction pattern of TaN. The $Ta_2N_{0.86}$ phase is indicated by the asterisks

Figure 5. Observed-calculated-difference (OCD) profile plot from the Rietveld refinement for ZrN. Observed data are shown in red (crosses), calculated (green solid line) and the difference between the two curves (pink). Black tickmarks correspond to peak positions of cubic ZrN

The diffraction pattern of synthesised Mo_2N in Figure 3 shows peaks corresponding to the planes which match with the pattern of Powder Diffraction File Database having the card No. 024-0768 with the most intense peaks occurring at diffraction angles, $2\theta = 37.6°$ and $43.05°$ which correspond to the (112) and (200) reflection planes, respectively. The diffraction at $2\theta = 40.5°, 58.6°, 73.6°, 87.6°$ and $101.4°$ can be identified as the $(111), (200), (211), (220)$ and (310) crystal planes of Mo (PDF#00-004-0809).

The peaks recorded in Figure 4 match those of hexagonal TaN (PDF#00-039-1485) with the presence of slight impurity of hexagonal $Ta_2N_{0.86}$ (PDF#01-089-5199).

It was observed that the routes used for the synthesis of Mn_4N, NbN, Mo_2N and TaN produced a nitrogen deficient nitrides of formula $Mn_2N_{0.86}$, $Nb_8N_{6.8}$, and $Ta_2N_{0.86}$, as second phases, which is likely these materials formed are sub-stoichiometric nitrogen. This low value may be due to the refractory nature of these metal nitrides. This may also correspond to some nitrogen sub-stoichiometry as many transition metal nitrides are interstitial compounds and are metal rich, which they are known to tolerate wide ranges in composition [17]. It should be noted that some nitrogen loss may occur prior to analysis.

ZrN and Li_3N have been synthesised and studied. Structural refinements performed against powder X-ray diffraction data were conducted using General Structure Analysis System (GSAS). The least-square refinements were carried out until the best fit was obtained between the entire observed powder diffraction patterns taken as a whole and the entire calculated patterns based on the published structures as starting models. The major parameters refined were scale factors, zero shifts, unit cells, Pseudo-Voigt peaks, shape, and profile parameters.

As-prepared ZrN was a fine, yellow/brown powder. In a typical synthetic method with an appropriate choice of conditions, the nonthermal plasma reaction generates crystalline phase-pure ZrN (PDF#03-065-9412). Most importantly, no oxide or hydroxide impurities have been detected.

Manually fitting the background using 12 coefficients gave the best fit. The experimental pattern fits well with the theoretical pattern as displayed in Figure 5. The main phase was indexed to a cubic cell (Space group No.225: $Fm\bar{3}m$). Rietveld refinement yielded lattice parameters of a=4.58093(4) Å and a cell volume of 96.131(2) $Å^3$.
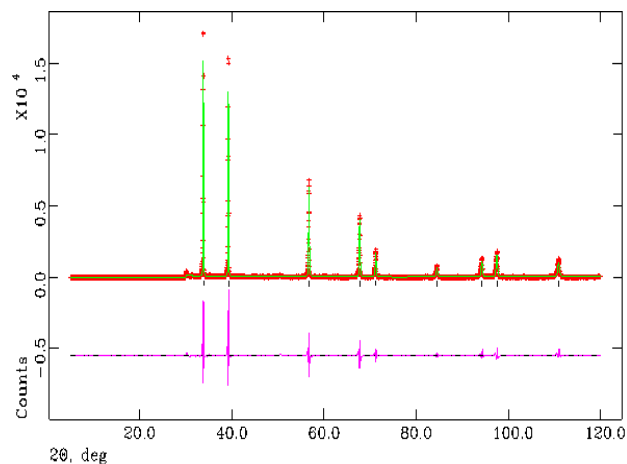
Selected Rietveld refinement data and atomic parameters are presented in Tables 1 and 2. Estimated standard deviation (esd) values are shown in parentheses.

**Table 1.** Crystallographic data obtained from the Rietveld refinement for ZrN powder

Chemical formula	ZrN
Crystal system	Cubic
Space group	$Fm\bar{3}m$ (225)
Lattice parameter, a /Å	4.58093(4)
Volume / $Å^3$	96.131(2)
Formula units, Z	4
Formula weight/ g mol^{-1}	356.154
Calculated density/ g cm^{-3}	6.152
No. of observations, parameters	5385, 25
R_{wp}, R_P	0.2933, 0.2379
χ^2	12.93

Table 2. Atomic parameters for ZrN powder

Atom	Wyckoff symbol	x	y	z	Occupancy	$U_{iso} \times 100/$ $Å^2$
N	4a	0	0	0	1	0.38(23)
Zr	4b	0.5	0.5	0.5	1	1.21(2)

The reaction between Li metal and nitrogen gas to form Li_3N occurred spontaneously. Li metal foil was left in a nitrogen-filled glovebox, and after 3 days of exposure, the color of the Li foil changed from white to black. The as-obtained powder was heated at 200°C for around 24 h to ensure a complete reaction. During the course of the experiment, N_2 gas was flowed through the furnace and paraffin bubbler heating the crucible allowed for reaction temperature 200°C to be reached. Once cooled, the crucible and its content were removed from the furnace and transferred to a glovebox where they were opened using pipe cutter, which allowed the crucible lid to be removed cleanly without polluting the sample. The black powder of Li_3N turned purple/red with lustrous effect after annealing process in the same atmosphere. The final powder was thoroughly mixed and ground together using an agate pestle and mortar. The crystallinity and phase purity of the annealing powder after grinding was then determined by powder X-ray diffraction.

All the diffraction peaks of the resulting powder can be readily indexed to alpha-Li$_3$N exhibiting strong intensity, indicating the high crystallinity of the powder sample. Weak peaks of Beta-Li$_3$N were additionally observed. This may be due to the pressure induced phase transformation during the grinding process [18]. No other impurities, such as LiOH and Li$_2$O, were detected by PXD due to its limited sensitivity.
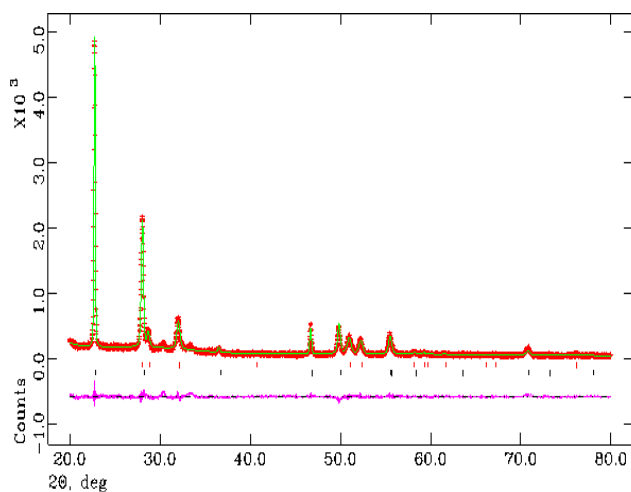
Figure 6. Observed-calculated-difference (OCD) profile plot from the Rietveld refinement for Li$_3$N powder. Observed data are shown in red (crosses), calculated in green (solid line) and the difference between the two curves (pink). Black tickmarks are reflections from α-Li$_3$N. The red tickmarks correspond to peak positions of β-Li$_3$N

The experimental powder X-ray diffraction data for synthesised Li$_3$N was refined via the Rietveld method in order to obtain weight percentage values for alpha and beta Li$_3$N phases. The models for each of the calculations were obtained from the online Inorganic Crystal Structure Database (ICSD) and PowderCell 2.4 was used to obtain a visual comparison between the experimental and theoretical models.

Table 3. Selected Rietveld refinement data from PXD data of synthesised Li$_3$N powder

Empirical formula		α-Li$_3$N	β-Li$_3$N
Crystal system		Hexagonal	Hexagonal
Space group		P6/mmm(191)	P63/mmc(194)
Lattice parameters/ Å	a	3.6447(1)	3.5724(3)
	c	3.8737(1)	6.3417(6)
Volume/Å^3		44.566(3)	70.091(13)
Formula units, Z		2	4
Formula weight/ g mol^{-1}		24.301	55.423
Calculated density/ g cm^{-3}		0.905	1.313
Phase fraction/ wt.%		70.37(15)	29.63(29)
No. of observations		3589	
No. of variables		44	
R$_{wp}$		0.1086	
R$_p$		0.0801	
χ^2		1.685	

The refinement was carried out using structural parameters of alpha-Li$_3$N in hexagonal symmetry [$Space\ group\ No.191: P6/mmm, ICSD\#34779$], and beta-Li$_3$N in hexagonal symmetry [$Space\ group\ No.194: P63/mmc, ICSD\#156889$]. The observed-calculated-difference (OCD) profile plot is shown in Figure 6. Selected Rietveld refinement data and atomic parameters are presented below in

Tables 3, 4 and 5. Estimated standard deviation (esd) values are shown in parentheses.

Rietveld refinement of the diffraction data yielded lattice parameters of a=3.6447(1), c=3.8737(1) for α-Li$_3$N, and a=3.5724(3), c=6.3417(6) for β-Li$_3$N. A cell volume of 44.566(3) and 70.091(13) were obtained, respectively. The agreement indices in the simulated pattern gives the best fit value of weighed R$_p$-R$_{wp}$ and goodness of fit-χ^2=1.685 with 70.37(15) % of α-Li$_3$N and 29.63(29) % of β-Li$_3$N phase fractions.

Table 4. Atomic parameters for α-Li$_3$N

Atom	Wyckoff symbol	x	y	z
Li1	1b	0	0	0.5
Li2	2c	0.3333	0.6667	0
N	1a	0	0	0

Occupancy	Uiso×100/ Å^2
0.573(9)	16.03(57)
0.812(5)	11.15(19)
0.647(3)	10.30(13)

Table 5. Atomic parameters for β-Li$_3$N

Atom	Wyckoff symbol	x	y	z
Li1	2b	0	0	0.25
Li2	4f	0.3333	0.6667	0.5915(15)
N	2c	0.3333	0.6667	0.25

Occupancy	Uiso×100/ Å^2
0.879(16)	6.63(52)
0.651(10)	7.80(33)
0.898(6)	10.26(20)

The diffuse reflectance is measured as a function of the wavelength of the incident radiation as in normal UV-Vis spectrometry within the operative range of 190-1300 nm.

The determination of the optical band gap is easily extrapolated from its absorption spectrum according to the process originally proposed by Tauc et al. [15], and David and Mott [16]. Tauc's plot proposes the proportionality between the band gap (E$_g$) and the absorption coefficient (α) of the material.

$$(\alpha h\nu)^{1/n} = A(h\nu - E_g) \qquad (1)$$

where, h is the Plank constant, ν is the light frequency and A is a proportionality constant depending on the properties of the material. n defined as power factor and its value depends on the nature of the optical transition probability [19]. The value of n derive from the description of the electronic bands through their wavelength in function of the imaginary part of the dielectric constant of the material [15].

According to the Kubelka-Munk theory [20, 21] and Tauc plot of $(F(R)h\nu)^{1/n}$ as a function of the incident radiation energy, the characteristic slop is fitted as a linear interpolation. The intersection of the slop with the x-axis ($h\nu$) directly provides the value of the band gap [22].

Optical band gaps obtained from the reflectance data on synthesised Mn$_4$N, NbN, Mo$_2$N, TaN, ZrN and Li$_3$N nitride materials were estimated to be 2.18 eV, 3 eV, 3.1 eV, 1.32 eV, 2.8 eV, and 1.95 eV, respectively, as shown in Figures 7, 8, 9, 10, 11 and 12.
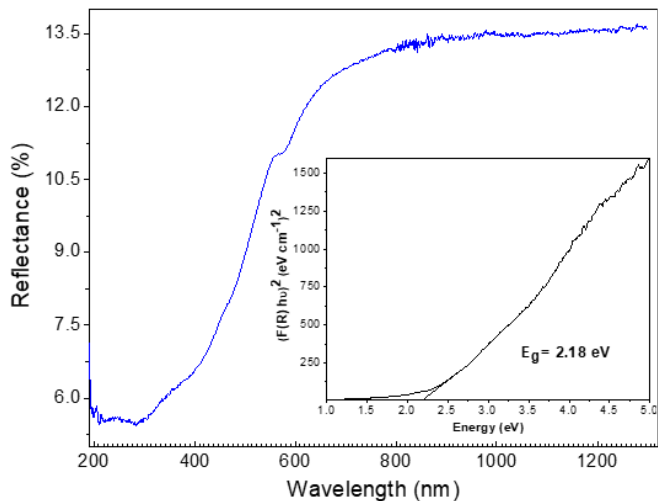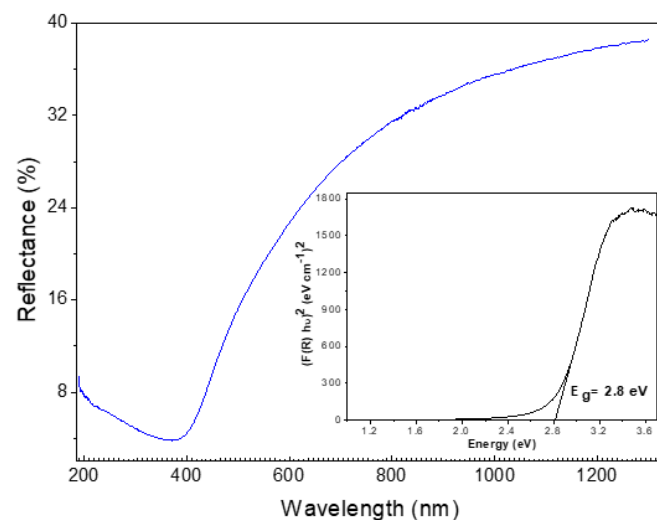
Figure 7. UV-Vis spectrum of Mn$_4$N with Tauc plot for band gap determination
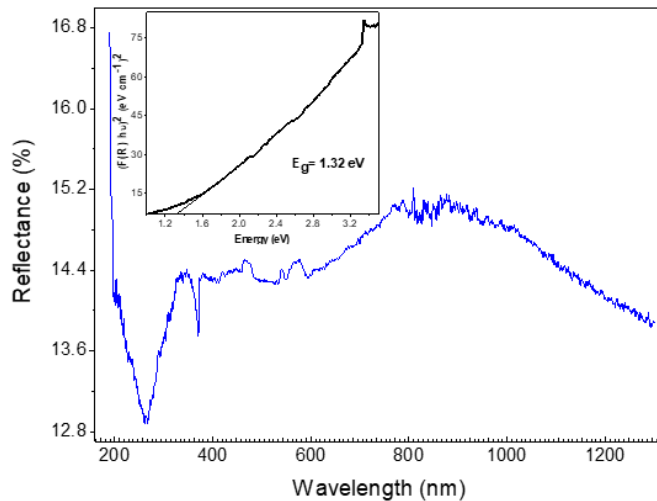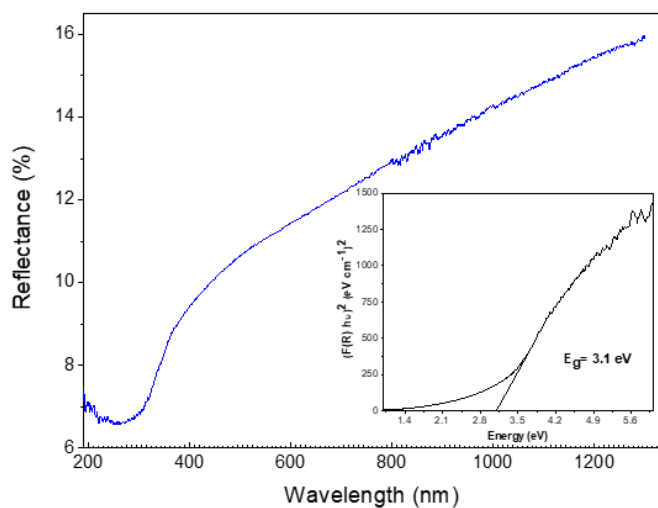

Figure 10. UV-Vis spectrum of TaN with Tauc plot for band gap determination
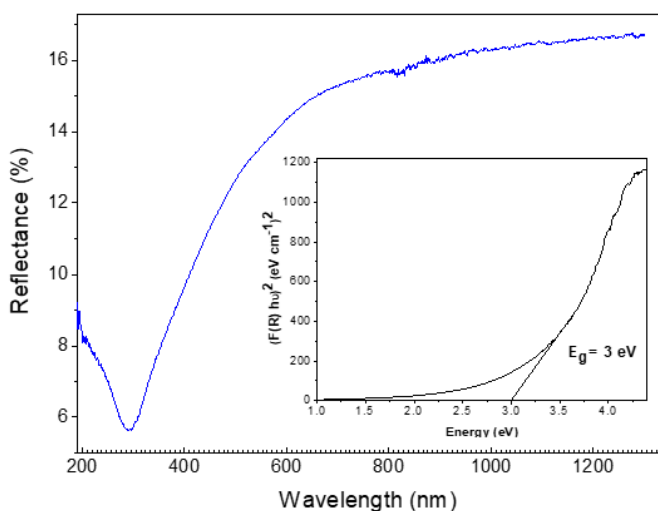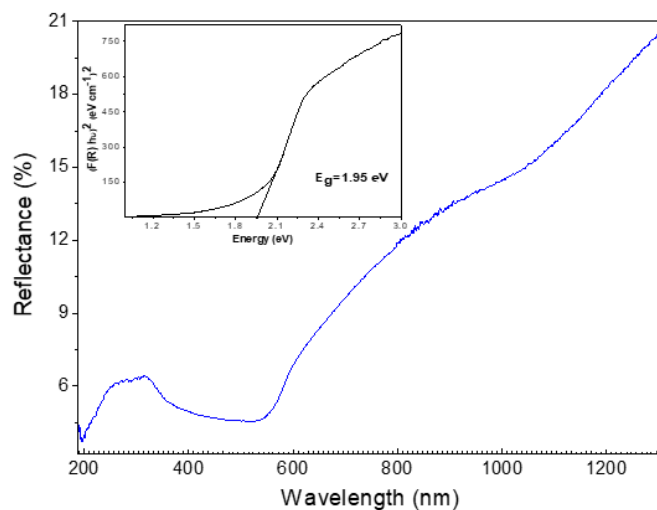

Figure 8. UV-Vis spectrum of NbN with Tauc plot for band gap determination

Figure 11. UV-Vis spectrum of ZrN with Tauc plot for band gap determination

Figure 9. UV-Vis spectrum of Mo$_2$N with Tauc plot for band gap determination

Figure 12. UV-Vis spectrum of Li$_3$N with Tauc plot for band gap determination

5. CONCLUSIONS

In the present study, it was demonstrated that the methods outlined, as under which nitride materials produced with high purity, were successfully applied. Some of the following important observations are:

(i) Additional of minor sub-stoichiometric nitrogen phases of formula $Mn_2N_{0.86}$, $Nb_8N_{6.8}$ and $Ta_2N_{0.86}$ have been detected by X-ray powder diffraction, which were probably formed prior to analysis. However, no evidence of any oxidation of the synthesised samples has been seen.

(ii) The Rietveld analysis based on the structure refinement has been adopted for precise determination of structural parameters. Nonthermal plasma reactor is considered the most convenient method leading to successful preparation of ZrN single phase with cubic structure. The Rietveld refinement analysis revealed also the high purity of synthesised Li_3N powder, with the formation of 70.37(15)% alpha-Li_3N and 29.63(29)% beta-Li_3N, suggesting phase transformation during the grinding process.

(iii) Band gaps of all samples were obtained by analysing their UV-Vis reflectance spectra.

REFERENCES

[1] Brese, N.E., O'Keeffe, M. (1992). Crystal chemistry of inorganic nitrides. In: Complexes, Clusters and Crystal Chemistry. Structure and Bonding, vol 79. Springer, Berlin, Heidelberg. https://doi.org/10.1007/BFb0036504

[2] Sun, W., Holder, A., Orvañanos, B., Arca, E., Zakutayev, A., Lany, S., Ceder, G. (2017). Thermodynamic routes to novel metastable nitrogen-rich nitrides. Journal of Chemistry of Materials, 29(16): 6936-6946. https://doi.org/10.1021/acs.chemmater.7b02399

[3] Thomas, A.M. (2017). Introducing DDEC 6 atomic population analysis: Part 3. Comprehensive method to compute bond orders. Journal of RSC Advances, 7(72): 45552-45581. https://doi.org/10.1039/C7RA07400J

[4] Thomas, A.M., Nidia, G.L. (2016). Introducing DDEC 6 atomic population analysis: Part 1. Charge portioning theory and methodology. Journal of RSC Advances, 6(53): 47771-47801. https://doi.org/10.1039/C6RA04656H

[5] Maintz, S., Deringer, V.L., Tchougréeff, A.L., Dronskowski, R. (2016). LOBSTER: A tool to extract chemical bonding from plane-wave based DFT. Journal of Computational Chemistry, 37(11): 1030-1035. https://doi.org/10.1002/jcc.24300

[6] Niewa, R., Jacobs, H. (1996). Journal of Chemical Reviews, 96: 2053.

[7] Niewa. R., DiSalvo. F.J. (1998). Journal of Chemical Reviews. Mater, 10: 2733.

[8] Akimasa, Y., Takashi, A., Ryoko, M., Yuzo, S. (1984). Journal of Bulletin of the Chemical Society of Japan, 57(6): 1582-1585.

[9] Choi, J.G., Brenner, J.R., Thompson, L.T. (1995).

Journal of Catalysis, 154: 33.

[10] Ma, C.H., Zhang, W.F., He, J.L., Zhu, H.M. (2007). Synthesis and characterization of tantalum nitride nanopowder prepared through homogeneous reaction. Journal of Transactions of Nonferrous Metals Society of China, 17: s556-s559.

[11] Palko, A.A., Ryon, A.D., Kuhn, D.W. (1958). The vapor pressures of zirconium tetrachloride and hafnium tetrachloride. Journal of Physical Chemistry, 62(3): 319-322. https://doi.org/10.1021/j150561a017

[12] Yajima, A., Segawa, Y., Matsuzaki, R., Saeki, Y. (1983). Reaction process of zirconium tetrachloride with ammonia in the vapor phase and properties of the zirconium nitride formed. Journal of Bulletin of the Chemical Society of Japan, 56(9): 2638-2642. https://doi.org/10.1246/bcsj.56.2638

[13] Larson, A.C., Von Dreele, R.B. (2000). The General Structure Analysis System. Los Alamos National Laboratories. Los Alamos. NM.

[14] Toby, B.H. (2001). EXPGUI, Graphical User Interfaces for GSAS. Journal of Applied Crystallography, 34: 210-213. https://doi.org/10.1107/S0021889801002242

[15] Tauc, J., Grigorovici, A., Vancu, A. (1966). Optical properties and electronic structure of amorphous germanium. Journal of Physica Status Solidi (b), 15(2): 627-637. https://dx.doi.org/10.1002/pssb.19660150224

[16] Davis, E.A., Mott, N.F. (1970). Conduction in non-crystalline systems V. Conductivity, optical absorption and photoconductivity in amorphous semiconductors. Journal of Philosophical Magazine, 22(179): 903-922. https://doi.org/10.1080/14786437008221061

[17] Parkin, I.P., Nartowski, A.M. (1998). Solid state metathesis routes to group IIIa nitrides: Comparison of Li_3N and Mg_3N_2 as nitriding agents. Journal of Polyhedron, 17(16): 2617-2622. https://doi.org/10.1016/S0277-5387(97)00454-3

[18] Sun, Y., Li, Y., Sun, J., Li, Y., Pei, A., Cui, Y. (2017). Stabilized Li_3N for efficient battery cathode prelithiation. Journal of Energy Storage Materials, 6: 119-124. https://dx.doi.org/10.1016/j.ensm.2016.10.004

[19] Zhao, Y., Li, C., Liu, X., Gu, F., Jiang, H., Shao, W., Zhang, Li., He, Y. (2007). Synthesis and optical properties of TiO_2 nanoparticles. Journal of Materials Letters, 61(1): 79-83. https://doi.org/10.1016/j.matlet.2006.04.010

[20] Kubelka, P., Munk, F. (1931). Ein Beitrag Zur Optik Der Farbanstriche. Journal of Zeitschrift für Technische Physik, 12: 593-601.

[21] Kubelka, P. (1948). New contributions to the optics of intensely light-scattering materials. Part I. Journal of the Optical Society of America, 38(5): 448-457. https://doi.org/10.1364/JOSA.38.000448

[22] Nowak, M., Kauch, B., Szperlich, P. (2009). Determination of energy band gap of nanocrystalline SbSI using diffuse reflectance spectroscopy. Journal of Scientific Instruments, 80(4): 046107. https://doi.org/10.1063/1.3103603